Editors' Suggestion

Quantum Microwave Parametric Interferometer

F. Kronowetter,[1,2,3,*] F. Fesquet,[1,2] M. Renger,[1,2] K. Honasoge,[1,2] Y. Nojiri,[1,2] K. Inomata,[4,5] Y. Nakamura,[4,6] A. Marx,[1] R. Gross,[1,2,7] and K.G. Fedorov[1,2,†]

[1] *Walther-Meißner-Institut, Bayerische Akademie der Wissenschaften, Garching 85748, Germany*
[2] *School of Natural Sciences, Technische Universität München, Garching 85748, Germany*
[3] *Rohde & Schwarz GmbH & Co. KG, Munich 81671, Germany*
[4] *RIKEN Center for Quantum Computing (RQC), Wako, Saitama 351-0198, Japan*
[5] *National Institute of Advanced Industrial Science and Technology, 1-1-1 Umezono, Tsukuba, Ibaraki 305-8563, Japan*
[6] *Department of Applied Physics, Graduate School of Engineering, The University of Tokyo, Bunkyo-ku, Tokyo 113-8656, Japan*
[7] *Munich Center for Quantum Science and Technology (MCQST), Munich 80799, Germany*

(Received 6 April 2023; revised 28 July 2023; accepted 3 August 2023; published 21 August 2023)

Classical interferometers are indispensable tools for the precise determination of various physical quantities. Their accuracy is bound by the standard quantum limit. This limit can be overcome by using quantum states or nonlinear quantum elements. Here, we present the experimental study of a nonlinear Josephson interferometer operating in the microwave regime. Our quantum microwave parametric interferometer (QUMPI) is based on superconducting flux-driven Josephson parametric amplifiers combined with linear microwave elements. We perform a systematic analysis of the implemented QUMPI. We find that its interferometric power exceeds the shot-noise limit and observe sub-Poissonian photon statistics in the output modes. Furthermore, we identify a low-gain operation regime of the QUMPI that is essential for optimal quantum measurements in quantum illumination protocols.

DOI: 10.1103/PhysRevApplied.20.024049

I. INTRODUCTION

As part of the second quantum revolution, various quantum technologies have matured to a level allowing their use in a plethora of practical applications [1,2]. In particular, the fields of quantum communication, metrology, and sensing have made great progress [2–5]. In metrology, the field of interferometry has been widely explored in terms of fundamental physics and resulted in a variety of technical breakthroughs [6–8]. Classical interferometers, such as the Mach-Zehnder interferometer, typically rely on the injection of a coherent state into one port of a beam splitter, while only vacuum fluctuations enter the second port [9]. Their phase sensitivity is limited by the shot noise of the coherent signal, also known as the standard quantum limit (SQL). The SQL results in a $1/\sqrt{N}$ scaling of the sensitivity limit, or, equivalently, in a $\sqrt{N}$ scaling of the signal-to-noise ratio (SNR), where N is the photon number of the input coherent state [10,11]. This linear interferometer sensitivity can be improved by coupling quantum states, such as squeezed states, into the second beam splitter port [10,12]. Alternatively, the SQL can be overcome by making use of nonlinear elements such as parametric amplifiers, leading to interactions between photons [3,13–15]. In principle, exploiting quantum correlations between photons in these states allows one to achieve the Heisenberg limit (HL) with a linear scaling of the SNR with respect to N [10,16]. While nonlinear interferometers have been investigated at optical frequencies, the microwave domain has so far remained largely unexplored due to relatively small energies of microwave photons with frequencies in the 1–10 GHz regime and the associated difficulty of single-photon detection [10,15,17,18]. Meanwhile, quantum microwave sensing and communication represent novel and rapidly growing fields, which promise groundbreaking fundamental experiments and applications [19–22].

In this article, we present an experimental realization of a nonlinear microwave interferometer, making use of Josephson-junction-based superconducting quantum circuits (see Fig. 1). This quantum microwave parametric interferometer (QUMPI) consists of two linear balanced microwave beam splitters and two nonlinear quantum devices in the form of flux-driven Josephson parametric

*fabian.kronowetter@wmi.badw.de
†kirill.fedorov@wmi.badw.de

amplifiers (JPAs). We experimentally characterize the QUMPI by injecting various Gaussian states and analyze its performance by comparing experimental results to predictions of an input-output theory model in terms of output photon numbers, interferometric power, and second-order correlation functions. We observe that the interferometric power of the QUMPI exceeds the SQL, which highlights the potential of our scheme in precision metrology [13]. With symmetric coherent signal inputs, our interferometer shows photon antibunching between the outputs. This is captured by a second-order cross-correlation function, $g_C^{(2)} < 1$, and reflects the nonclassical nature of the QUMPI. For the specific operating point with equal phase-sensitive gain amplitudes, $G_1 = G_2 = G$, of the JPAs and orthogonal amplification angles, $\gamma_1 = \gamma_2 + \pi/2$, the input-output operator relation of the circuit coincides with that of an SU(1,1) interferometer [10]. The QUMPI can also be used for analog Bell measurements in microwave quantum teleportation [19]. In the low-gain operating regime, $G \gtrsim 1$, the QUMPI realizes an effective two-mode, phase-conjugate signal mixing, which is an integral part of joint receivers for quantum radar schemes [23–26]. All these findings demonstrate the practical versatility and fundamental potential of the considered scheme.

II. EXPERIMENT

In Fig. 1(a), we present the idea of the QUMPI. Input signals at ports In1 and In2 are split and subsequently fed into JPA1 and JPA2. Then, the nonlinearly amplified signals from the JPAs interfere and leave the circuit at ports Out1 and Out2. Figure 1(b) shows a detailed circuit layout of our experiment. We employ two symmetric hybrid rings (HRs) as microwave beam splitters and two superconducting flux-driven JPAs. The latter are operated at a frequency of $\omega_0/2\pi = 5.48$ GHz. Experimental bandwidths of JPA1 and JPA2 are 2 and 10 MHz, respectively. Low-loss microwave cryogenic circulators are used to separate the incoming and outgoing signals of the JPAs [cf. Fig. 1(c)]. We operate both JPAs in the phase-sensitive amplification regime by pumping them at twice the resonance frequency, $\omega_p = 2\omega_0$ [27,28]. The microwave interferometer arms are tailored to have identical lengths with an accuracy of 1 mm. At the carrier frequency of around 5.5 GHz, the corresponding wavelength in our superconducting cable is approximately 38 mm. Given the interferometer arm accuracy in comparison with the signal wavelength, microwave signals traveling along different interferometer paths do not acquire a significant relative, path-induced phase shift. However, the overall phase difference also depends on JPA-induced phase shifts, which can be adjusted by fine-tuning the JPA operation frequency with an external magnetic flux [28]. The output state tomography relies on heterodyne measurements with a field-programmable-gate-array- (FPGA) based digitization setup [29,30]. After digital down-conversion and filtering, we use a reference-state reconstruction method to extract statistical field quadrature moments and reconstruct a covariance matrix of the quantum states at a certain reference point [29–31]. This reference point can be defined by performing a Planck spectroscopy that provides a precise *in situ* photon-number calibration of the output lines [32].

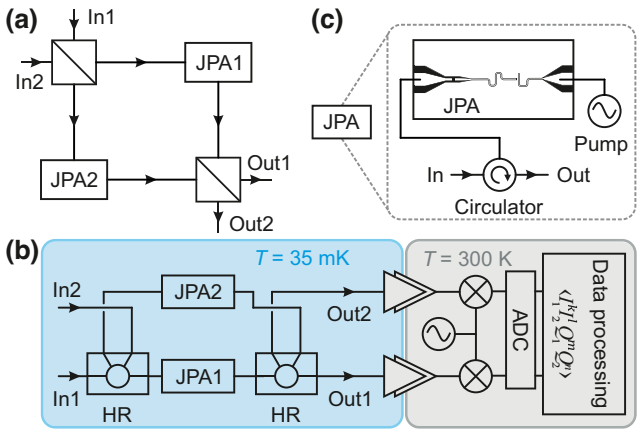

FIG. 1. (a) General scheme of the QUMPI. (b) Details of the experimental setup consisting of a 180° hybrid ring (HR), which splits and symmetrically superimposes two incoming signals from ports In1 and In2, two JPAs for phase-sensitive amplification, and a second 180° HR, which completes the nonlinear interferometer. Output two-mode signals are detected with a heterodyne microwave receiver, followed by analog-to-digital (ADC) conversion, and digitally processed to extract statistical signal moments. The latter enable a full state tomography. (c) A circulator separates the incoming and outgoing signals for each JPA.

III. RESULTS AND DISCUSSION

A systematic study of the QUMPI requires careful circuit calibration and a precise control of the JPAs. First, we detune both JPAs from the intended operation frequency and switch our interferometer into the linear regime. We then perform Planck spectroscopy of our system by injecting a thermal state generated by a heatable attenuator at one input and vacuum at the other, as illustrated in Fig. 2(a) [32]. Figures 2(b) and 2(c) show the corresponding experimental results. We observe both constructive and destructive interference of the broadband thermal signals, as expected in a symmetric linear interferometer. Thermal-signal injection at In1 (orange points) results in the temperature dependence of P_1, while P_2 remains independent of T due to destructive interference. The inverted case of thermal-signal injection at In2 (purple points) demonstrates the system symmetry, which is reflected in $P_2(T)$ and a T-independent response of P_1.

As a second part of the calibration routine, we tune both JPAs to the same resonance frequency of $\omega_0/2\pi =$

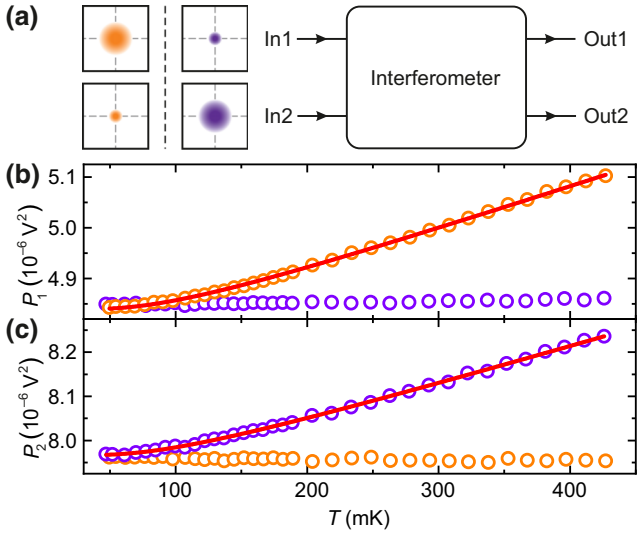

FIG. 2. Planck spectroscopy of the interferometer in the linear regime for output channel powers (b) P_1 at Out1 and (c) P_2 at Out2. Orange points correspond to thermal-state injection at In1 and vacuum at In2, and purple points correspond to the inverted case of thermal-state injection at In2 and vacuum state at In1, as depicted schematically in the quadrature planes in (a). The temperature dependence of P_1 (P_2) for orange (purple) data points yields the photon-number calibration for the interferometer and verifies its functionality. The corresponding error bars are smaller than the symbol size. The solid red lines represent fits based on Planck's law.

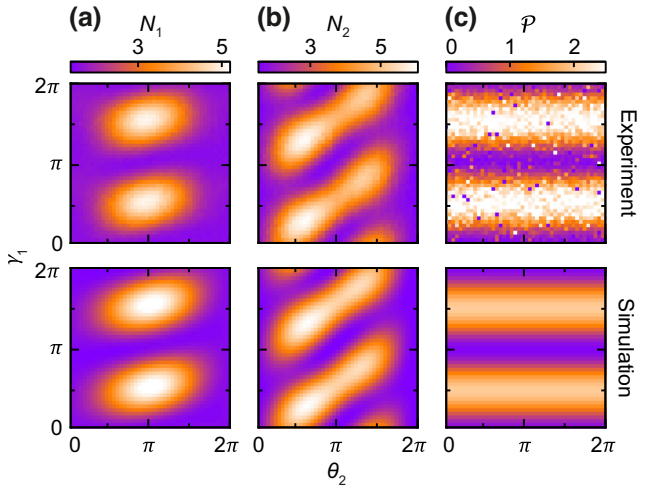

FIG. 3. Interferometer measurements with coherent signals applied to In1 and In2. The corresponding displacement amplitudes are $|\alpha_1| = |\alpha_2| = 0.83(5)$, and the displacement angle θ_1 is fixed to 0.64π, while θ_2 varies from 0 to 2π. Both JPAs are operated as squeezers with the average gain $\overline{G}_{1,2} = 7.73$ dB and squeezing angle γ_1 varying from 0 to 2π, while $\gamma_2 = 0$. Top row shows the experimentally reconstructed photon numbers (a) N_1 and (b) N_2 at ports Out1 and Out2, respectively, as a function of θ_2 and γ_1. (c) Interferometric power $\mathcal{P}$ of the QUMPI illustrating the two-mode state probe capabilities.

5.48 GHz. This step converts the QUMPI into the nonlinear regime. The JPA response is controlled via magnitude and phase of the coherent pump tone. Since we expect the best interferometric performance for a balanced gain of $G_1 = G_2$ [10], we inject vacuum states at both circuit inputs and pump the JPAs with varying magnitude and phase [29]. We balance the produced two-mode states at the interferometer output by minimizing asymmetries of the local output modes. These asymmetries result in squashed variances $\sigma^2_{s,i}$ and amplified variances $\sigma^2_{a,i}$ ($i = 1, 2$ denote path 1 and path 2, respectively) of the local phase space distributions. We define a balancing criterion as $\mathcal{B} = (\sigma^2_{s,1}/\sigma^2_{a,1})(\sigma^2_{s,2}/\sigma^2_{a,2})$. For our system, we observe $\mathcal{B}$ reaching values of around 0.91, close to the optimum of $\mathcal{B} = 1$ (see Appendix C for details). Finite asymmetries and insertion losses of the HRs, as well as the nonidentical noise properties of the JPAs, limit the balancing.

After the calibration, we investigate the nonlinear interferometer response to coherent signals applied to both input ports, In1 and In2, with a photon number of $|\alpha_1|^2 = |\alpha_2|^2 = 0.69(7)$, where $|\alpha_i|$ ($i = 1, 2$) are the respective displacement amplitudes [33]. We fix one coherent displacement angle, $\theta_1 = 0.64\pi$, while varying the other, θ_2. Both JPAs are operated with an average gain $\overline{G}_{1,2} = 7.73$ dB and an average number $\overline{n}_{1,2} = 0.238$ of added noise photons referred to the JPA inputs. The JPA2 squeezing angle, γ_2, is fixed to 0 and we vary γ_1. We compare the acquired data with a theoretical model of our system based on the input-output formalism (see Appendix B for more details). Figures 3(a) and 3(b) show the photon numbers $N_i = \langle \hat{a}_i^\dagger \hat{a}_i \rangle$ at the respective outputs Out1 and Out2. Here, $\hat{a}_i^\dagger$ ($\hat{a}_i$) is the photon creation (annihilation) operator. The bottom row of Fig. 3 shows the model prediction. The common color bars for each column underline good quantitative agreement between experiment and theory. As a model quality metric, we introduce the normalized distance $d(\mathbf{x}) := \sum_{i=1}^{M} \sum_{j=1}^{N} |a_{ij} - b_{ij}|/|a_{ij}|$ between the respective data matrices a_{ij} and model matrices b_{ij} of dimension $M \times N$ with respect to a quantity $\mathbf{x}$. The corresponding distances are $d(N_1) = 7.6\%$ and $d(N_2) = 6.5\%$. Since our model intrinsically corresponds to a nonlinear interferometer, this agreement confirms that our experimental system acts as such. The asymmetry in the patterns between Figs. 3(a) and 3(b) stems from the nonlinear character of our interferometer.

Next, we evaluate the interferometric power (IP) of the QUMPI. For a bipartite quantum probe state, the IP defines the worst-case precision of a parameter estimation, where the corresponding parameter experiences unitary dynamics in one of the two subsystems (e.g., a phase shift of the signal in one interferometer arm) [34]. The respective IP is

defined as

$$\mathcal{P}(\rho_{AB}) = \tfrac{1}{4} \inf_{\hat{U}_A} \mathcal{F}(\rho_{AB}^{\Phi,\hat{U}_A}), \tag{1}$$

where ρ_{AB} is the two-mode probe state, $\hat{U}_A$ is an arbitrary unitary transformation of the subsystem A, $\mathcal{F}$ is the quantum Fisher information, and Φ is the corresponding estimator [34,35]. Remarkably, the IP provides a measure of bipartite discord-type correlations for Gaussian states beyond pure entanglement [34,36]. We apply the expressions from Ref. [34] to our theory model, as well as to the reconstructed experimental covariance matrices, in order to extract the IP of the QUMPI. Figure 3(c) depicts both the experimental and theoretical IPs as a function of θ_2 and γ_1. The data in Fig. 3(c) are independent of θ_2, since $\mathcal{P}$ is invariant under local unitary operations [34]. Furthermore, $\mathcal{P}$ goes to zero for parallel amplification angles $\gamma_1 = \gamma_2 + n\pi$ $(n = 1, 2, \ldots)$, where output states become separable, and is maximal for orthogonal amplification, where the states are entangled. In this context, the SQL sets an upper bound $\mathcal{P}_{\mathrm{SQL}} = N$ for separable two-mode probe states, where N is the mean photon number in the probing subsystem. For pure two-mode squeezed states, $\mathcal{P}$ saturates at the HL with $\mathcal{P}_{\mathrm{HL}} = N(N+1)$ [34]. The simulated IP reproduces the experimental data, but with a noticeably smaller maximum value, as can be seen from Fig. 3(c) and $d(\mathcal{P}) = 47.0\%$. We attribute this deviation to possible misestimates of losses in the underlying photon-number calibration. Both, maximum theoretical ($\mathcal{P}_{\mathrm{theory}}/\mathcal{P}_{\mathrm{SQL}} = 1.38$) and experimental ($\mathcal{P}_{\mathrm{exp}}/\mathcal{P}_{\mathrm{SQL}} = 1.70$) values exceed the SQL but do not reach the HL ($\mathcal{P}_{\mathrm{theory}}/\mathcal{P}_{\mathrm{HL}} = 0.58$, $\mathcal{P}_{\mathrm{exp}}/\mathcal{P}_{\mathrm{HL}} = 0.65$). The presence of finite noise in the system prevents reaching an IP closer to the HL. We note, however, that $\mathcal{P}_{\mathrm{exp}} > \mathcal{P}_{\mathrm{SQL}}$ provides direct evidence that the QUMPI exceeds the $\sqrt{N}$ scaling of the SNR, since $\mathrm{SNR} \propto \sqrt{\mathcal{P}}$.

In order to study correlation properties and related intensity fluctuation statistics of the QUMPI, we analyze the zero-delay-time second-order correlation function, $g^{(2)}(0)$, for the single-mode fields at the interferometer outputs, as well as the cross-correlations between the outputs [37]. For the two-mode fields, the respective autocorrelation function, $g_i^{(2)}(0)$, can be written as

$$g_i^{(2)}(0) = \frac{\langle \hat{a}_i^\dagger \hat{a}_i^\dagger \hat{a}_i \hat{a}_i \rangle}{\langle \hat{a}_i^\dagger \hat{a}_i \rangle^2}, \tag{2}$$

where $i = 1, 2$. The associated second-order cross-correlation function, $g_{\mathrm{C}}^{(2)}(0)$, can be expressed as

$$g_{\mathrm{C}}^{(2)}(0) = \frac{\langle \hat{a}_1^\dagger \hat{a}_1^\dagger \hat{a}_1 \hat{a}_1 \rangle + \langle \hat{a}_2^\dagger \hat{a}_2^\dagger \hat{a}_2 \hat{a}_2 \rangle + 2\langle \hat{a}_1^\dagger \hat{a}_1 \hat{a}_2^\dagger \hat{a}_2 \rangle}{(\langle \hat{a}_1^\dagger \hat{a}_1 \rangle + \langle \hat{a}_2^\dagger \hat{a}_2 \rangle)^2}. \tag{3}$$

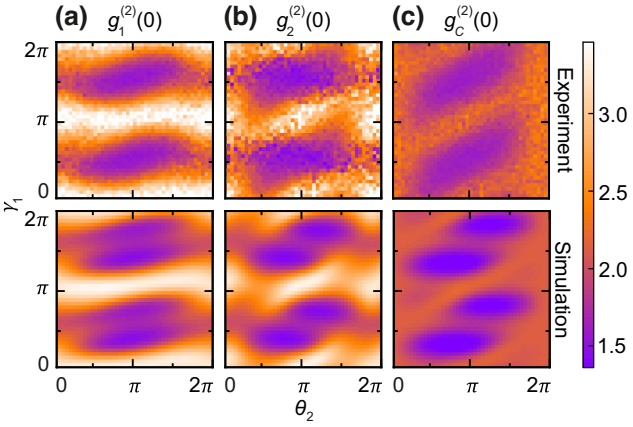

FIG. 4. Second-order correlation analysis of the QUMPI. Single-mode second-order correlation functions, $g_1^{(2)}(0)$ and $g_2^{(2)}(0)$, at the interferometer ports (a) Out1 and (b) Out2. (c) Second-order cross-correlation function, $g_{\mathrm{C}}^{(2)}(0)$, between ports Out1 and Out2. The experimental parameters are identical to those in Fig. 3.

The experimentally obtained data for $g_1^{(2)}(0)$, $g_2^{(2)}(0)$, and $g_{\mathrm{C}}^{(2)}(0)$ as a function of θ_2 and γ_1 are depicted in Fig. 4. The bottom row shows the respective theoretical predictions [38]. Our model sufficiently well reproduces the experimental observations with $d[g_1^{(2)}(0)] = 8.6\%$, $d[g_2^{(2)}(0)] = 10.4\%$, and $d[g_{\mathrm{C}}^{(2)}(0)] = 7.8\%$, although some fine features are not resolved in the experimental data. In accordance with the model, the local output modes show correlation functions indicating photon bunching, $g_1^{(2)}(0), g_2^{(2)}(0), g_{\mathrm{C}}^{(2)}(0) > 1$.

To further explore the QUMPI, we experimentally investigate $g_{\mathrm{C}}^{(2)}(0)$ as a function of the displacement amplitude of the incident coherent states. We observe that, for sufficiently large displacement amplitudes, $|\alpha_1|$ and $|\alpha_2|$, and equal displacement angles, $\theta_1 = \theta_2$, $g_{\mathrm{C}}^{(2)}(0)$ indicates antibunching between the interferometer outputs, providing evidence for nonclassical correlations between them [38]. In Fig. 5(a), we show $g_{\mathrm{C}}^{(2)}(0)$ predicted by our theoretical model. For the experimentally relevant model parameters, most importantly the adapted average JPA gain $\overline{G}_{1,2} = 4.06$ dB, Fig. 5(a) shows that $|\alpha_1|^2, |\alpha_2|^2 > 5$ is required to realize nonlocal photon antibunching, $g_{\mathrm{C}}^{(2)}(0) < 1$. Figure 5(b) shows the experimental data of $g_{\mathrm{C}}^{(2)}(0)$ as a function of $|\alpha|^2 = |\alpha_1|^2 = |\alpha_2|^2$. The blue line is a cut along the main diagonal of Fig. 5(a). The inset shows an expanded view of the region where the data points for $g_{\mathrm{C}}^{(2)}(0)$ drop below the classical limit. Our theory model suggests that the minimal coherent photon number $|\alpha|^2 = |\alpha_1|^2 = |\alpha_2|^2$ required to achieve $g_{\mathrm{C}}^{(2)}(0) < 1$ increases with increasing JPA gain, while $g_{\mathrm{C,min}}^{(2)}(0)$ converges towards unity for large JPA gain. At the same time,

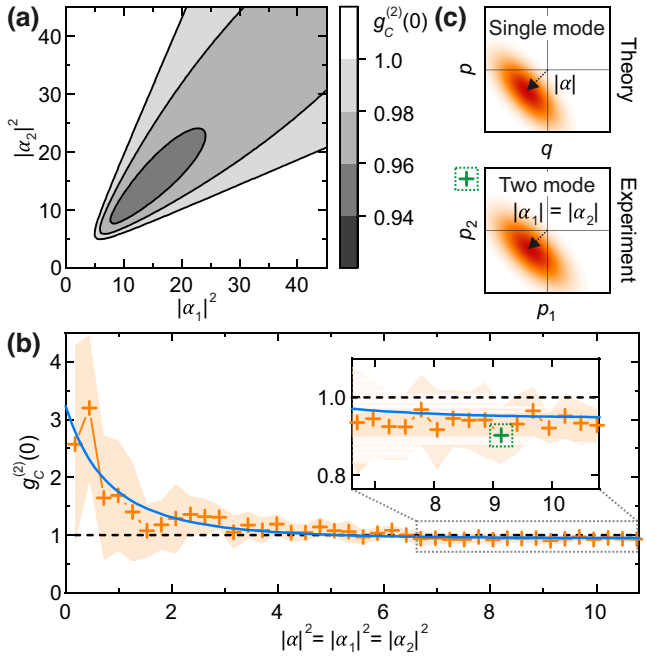

FIG. 5. Intensity cross-correlations, $g_C^{(2)}(0)$, of the interferometer output fields for variable displacement amplitudes of coherent input signals. (a) Model predictions as a function of the number of coherent photons $|\alpha_1|^2$ and $|\alpha_2|^2$ ($\theta_1 = \theta_2 = 0.81\pi$) entering the circuit at In1 and In2, respectively. (b) Experimental results for $g_C^{(2)}(0)$ (orange crosses with standard deviation shown in shaded orange) as a function of the symmetrically varied displacement amplitudes. The blue line depicts the theoretical prediction. The black dashed line illustrates the classical limit of $g_C^{(2)}(0) = 1$. (c) Analogy between Wigner functions of single-mode (theory) and two-mode [experiment; green cross from (b)] displaced squeezed states exhibiting $g^{(2)}(0) < 1$ ($g_C^{(2)}(0) < 1$).

$g_C^{(2)}(0)$ becomes more robust towards noise with increasing JPA gain.

Remarkably, for the specific operating point of the JPAs with equal gain and orthogonal amplification angles, the input-output relations of the QUMPI simplify to

$$\begin{aligned} \hat{b}_1 &= \sqrt{G_{\text{eff}}}\,\hat{a}_1 + \sqrt{G_{\text{eff}} - 1}\,\hat{a}_2^\dagger, \\ \hat{b}_2 &= \sqrt{G_{\text{eff}}}\,\hat{a}_2 + \sqrt{G_{\text{eff}} - 1}\,\hat{a}_1^\dagger, \end{aligned} \tag{4}$$

with the effective gain $\sqrt{G_{\text{eff}}} = \cosh(r)$ and the JPA squeezing factor $r = r_1 = r_2$ according to the JPA gain $G = \exp(2r)$. The input and output modes are described by bosonic operators $\hat{a}_1, \hat{a}_2$ and $\hat{b}_1, \hat{b}_2$, respectively. The relations in Eq. (4) coincide with those describing the so-called Josephson mixer, which can be utilized for producing microwave EPR states [19,21]. For low effective gain values, $G_{\text{eff}} \simeq 1$, our interferometer can be applied in a quantum illumination detection scheme for achieving a 3-dB advantage in the error exponent over the ideal classical counterpart [23–25]. Quantum illumination has been primarily investigated for optical frequencies [39–41], but the recent complete realization of a quantum microwave radar has sparked renewed interest in quantum microwave sensing [22]. Interestingly, the input-output relations in Eq. (4) also coincide with those of an SU(1,1) interferometer, with the exception that the coefficients, G_{eff} and $(G_{\text{eff}} - 1)$, enter linearly in the SU(1,1) implementation [10]. This difference is related to the fact that the parametric amplifiers are connected in series for the conventional SU(1,1) implementation, whereas the JPAs in the QUMPI are arranged in a parallel configuration.

IV. CONCLUSION

We have realized and systematically analyzed a quantum microwave parametric interferometer. We have performed a detailed investigation of the input-output relations of our QUMPI device with coherent and thermal input states. Our experimental results can be well explained by using a theoretical model based on the input-output quantum formalism. As part of our study, we have demonstrated nonlocal photon antibunching at the QUMPI outputs, characterized by $g_C^{(2)}(0) < 1$ for coherent input states. The investigated circuit is expected to be useful in many applications ranging from quantum-enhanced interferometry to mode mixing, as part of a joint quantum receiver in quantum sensing experiments [23,42]. Furthermore, our findings open a new avenue towards quantum enhanced nonlinear interferometers in the fast-evolving field of superconducting circuits operating in the microwave regime. Remarkably, current dark matter axion search experiments focus on the frequency range from 1 to 25 GHz and rely on readout by quantum limited amplifiers [43]. To this end, the QUMPI could find applications in related dark matter axion search experiments [44].

ACKNOWLEDGMENTS

We acknowledge support from the German Research Foundation via Germany's Excellence Strategy (EXC-2111-390814868), the German Federal Ministry of Education and Research via the project QUARATE (Grant No. 13N15380), JSPS KAKENHI (Grant No. 22H04937), and JST ERATO (Grant No. JPMJER1601). This research is part of the Munich Quantum Valley, which is supported by the Bavarian state government with funds from the Hightech Agenda Bayern Plus.

APPENDIX A: EXPERIMENTAL SETUP

A detailed scheme of the setup is shown in Fig. 6. The experiment has been performed in a custom-built wet dilution cryostat. A Zurich Instruments HDAWG 750-MHz arbitrary waveform generator provides modulation pulses to radio-frequency (rf) sources (R&S SGS100A) and for synchronizing the FPGA (model NI PXIe 7972). The rf

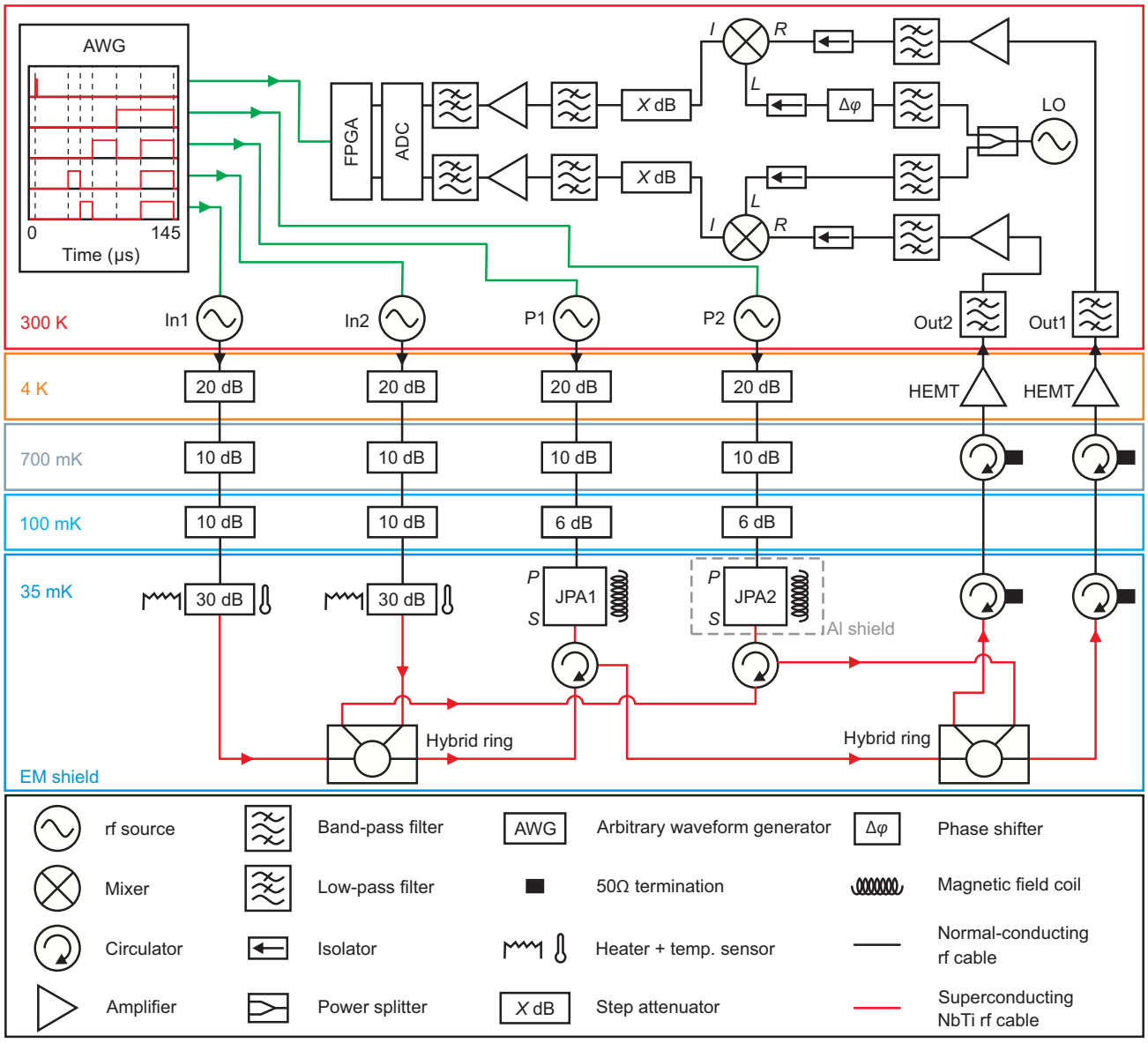

FIG. 6. Schematic of the measurement setup. The output signals are amplified and filtered in subsequent steps, down-converted, and digitized. An arbitrary waveform generator (AWG) creates a pulse sequence for the individual rf sources and the FPGA, which is required for the reference-state reconstruction [29].

sources are referenced to each other in a daisy chain configuration at a frequency of 1000 MHz starting with the rf source connected to In2. This source, the AWG, and the FPGA are synchronized at a frequency of 10 MHz by means of a rubidium frequency standard (Stanford Research Systems FS725). The different input lines (In1, In2, P1, P2) are sequentially attenuated at various temperature stages. The coldest attenuator of In1 (In2) is thermally coupled to a 100-Ω heater and a RuO_2 temperature sensor. At the same time, the attenuator is only weakly coupled to the mixing chamber plate of the dilution refrigerator. This allows for a precise proportional-integral-derivative temperature control of the coldest attenuators, while all other components can remain stable at a base temperature of $T = 35$ mK. The photon numbers in the reconstructed states are calibrated using Planck spectroscopy [32]. For that, we vary the temperature of a heatable 30-dB attenuator between 50 and 430 mK. The heatable attenuator serves as a self-calibrated, black-body photon source. This way we can link the detected voltage at the FPGA to the set temperature or, equivalently, to a thermal photon number in a microwave signal emitted from the heatable attenuator [32]. The sample stage is surrounded by a Cryoperm shield to protect it from magnetic stray fields. In

addition, JPA2 is enclosed in a superconducting Al shield in order to avoid crosstalk between superconducting magnetic coils mounted onto the two JPAs. These magnetic field coils generate an adjustable external magnetic field that enables tuning the operating frequency of the JPAs. Because of the low signal level, both signals at the output of the cryogenic sample stage need amplification in multiple stages starting with a cryogenic high-electron-mobility transistor (HEMT) amplifier and subsequent additional room-temperature amplifiers. Frequency-resolved measurements are performed using a vector network analyzer (not shown).

The tomography of quantum microwave states is performed using a heterodyne receiver setup and data processing similar to previous experiments described in Refs. [5,19,31,37]. Output signals at the operating frequency of 5.48 GHz are down-converted to an intermediate frequency of 11 MHz using image rejection mixers in combination with a local oscillator (LO) driven at 5.491 GHz. After the down-conversion, the signal power is adjustable by step attenuators in order to balance the two receiver lines. This attenuation also prevents compression effects in the subsequent amplification. After amplification and filtering, the down-converted signals are digitized by a transceiver adapter module (NI 5782-02) and processed in the FPGA. After digital down-conversion, the dc signals are further filtered by using a digital finite-impulse-response filter with a full bandwidth of 400 kHz. From the filtered and digitized data we compute the quadrature moments $\langle I_1^n Q_1^m I_2^k Q_2^l \rangle$ with $n, m, k, l \leq 4$. We assume that all reconstructed states are Gaussian, i.e., that they are represented by a Gaussian characteristic function in the signal quadrature phase space and can be entirely described by first- and second-order moments of the quadrature operators [34]. This assumption can be verified by calculating third- and fourth-order cumulants that are expected to vanish for Gaussian states [45]. If these cumulants are much smaller than the first- and second-order cumulants, we conclude that the Gaussian-state approximation is appropriate. The JPA squeezing angles are set via a phase-locked loop, where in each measurement cycle the actual squeezing orientation γ_i^{exp} $(i = 1, 2)$ is extracted from the quadrature moments of the signals emitted from the respective JPA. Next, the phase of the corresponding JPA pump signal is adjusted by $2\Delta\gamma_i$, where $\Delta\gamma_i$ is the difference between the actual angle γ_i^{exp} and the target angle γ_i^{target}. The respective phases of the coherent input tones are stabilized in a similar way by computing $\Delta\theta_i = \theta_i^{\text{exp}} - \theta_i^{\text{target}}$ and corrected by $\Delta\theta_i$. For independent adjustment of each rf source, the AWG produces a pulse sequence that drives each source twice per sequence: first for individual phase adjustment and the second time for data acquisition. A general scheme of the AWG pulse sequence is depicted in the inset of Fig. 6.

APPENDIX B: THEORETICAL MODEL

The nonlinear interferometer is modeled in a stepwise approach as a sequence of different operations, as depicted in Fig. 7. Since the thermal population of our states with a frequency of $\omega/2\pi = 5.48$ GHz at an effective temperature of $T \simeq 50$ mK is small $[n_{\text{th}} = 1/(\exp(\hbar\omega/k_B T) - 1) \approx 5 \times 10^{-3} \ll 1]$, we assume vacuum fluctuations as the variance of both signal inputs. The initial coherent state $\hat{a}_i$ $(i = 1, 2)$ with complex displacement amplitude α_i is modeled by applying the displacement operator $\hat{D}(\alpha_i)$ to vacuum $\hat{v}_i$:

$$\hat{a}_i = \hat{v}_i + \alpha_i. \tag{B1}$$

First, the signals of the two input lines are superimposed at a 180° HR, which we model as

$$\hat{B}_i^\dagger \begin{pmatrix} \hat{a}_1 \\ \hat{a}_2 \end{pmatrix} \hat{B}_i = \frac{1}{\sqrt{2}} \begin{pmatrix} -1 & 1 \\ 1 & 1 \end{pmatrix} \begin{pmatrix} \hat{a}_1 \\ \hat{a}_2 \end{pmatrix} \tag{B2}$$

with $i \in \{1, 2\}$. The losses due to insertion, connectors, and cable attenuation are modeled with a nonunitary operation

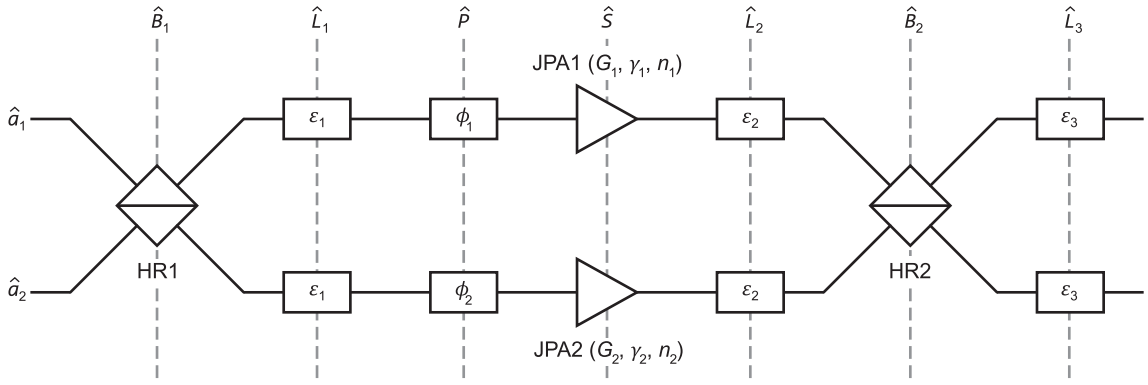

FIG. 7. Scheme of the theoretical model of the interferometer circuit. The incoming modes $\hat{a}_1$ and $\hat{a}_2$ sequentially undergo various transformations, as indicated by the vertical dashed lines. The final states are reconstructed after operation $\hat{L}_3$.

according to

$$\hat{L}_j^\dagger \begin{pmatrix} \hat{a}_1 \\ \hat{a}_2 \end{pmatrix} \hat{L}_j = \begin{pmatrix} \sqrt{1-\varepsilon_j}\,\hat{a}_1 + \sqrt{\varepsilon_j}\,\hat{v}_1 \\ \sqrt{1-\varepsilon_j}\,\hat{a}_2 + \sqrt{\varepsilon_j}\,\hat{v}_2 \end{pmatrix} \tag{B3}$$

with $j \in \{1,2,3\}$. The phase ϕ_i that is acquired by the signals in each interferometer arm is modeled as

$$\hat{P}^\dagger \begin{pmatrix} \hat{a}_1 \\ \hat{a}_2 \end{pmatrix} \hat{P} = \begin{pmatrix} e^{i\phi_1} & 0 \\ 0 & e^{i\phi_2} \end{pmatrix} \begin{pmatrix} \hat{a}_1 \\ \hat{a}_2 \end{pmatrix}. \tag{B4}$$

Next, the two JPAs perform a phase-sensitive amplification that we model by a squeezing operator according to

$$\hat{S}^\dagger \begin{pmatrix} \hat{a}_1 \\ \hat{a}_2 \end{pmatrix} \hat{S} = \begin{pmatrix} (\hat{a}_1 + \zeta_1)\cosh r_1 - (\hat{a}_1^\dagger + \zeta_1^*)e^{-2i\gamma_1}\sinh r_1 \\ (\hat{a}_2 + \zeta_2)\cosh r_2 - (\hat{a}_2^\dagger + \zeta_2^*)e^{-2i\gamma_2}\sinh r_2 \end{pmatrix}, \tag{B5}$$

where the JPA gain G_i is related to the squeezing parameter r_i via $G_i = e^{2r_i}$. The respective squeezing angle is denoted by γ_i. The noise added by the two JPAs is taken into account by introducing a random classical variable ζ_i that fulfills $\langle \zeta_i \zeta_i^* \rangle = n_i(G_i)$ and $\langle \mathrm{Re}(\zeta^2) \rangle = \langle \mathrm{Im}(\zeta^2) \rangle = n_i(G_i)/2$. Note that the noise depends on the respective gain [46]. For reliable analysis of G_i and n_i, we reconstruct the corresponding quantum states at the output of the second HR in a frame of the AWG pulsing scheme, when only JPA1 (JPA2) is driven, as depicted in Fig. 6. The full transformation of the circuit is given by the combined operator

$$\hat{F} = \hat{L}_3 \hat{B}_2 \hat{L}_2 \hat{S} \hat{P} \hat{L}_1 \hat{B}_1. \tag{B6}$$

Consequently, the final state $|\Psi\rangle$ can be expressed as [47]

$$|\Psi\rangle = \hat{F}|\alpha_1;\alpha_2\rangle. \tag{B7}$$

The signal moments of the circuit outputs $\hat{b}_i$ are given by

$$\begin{pmatrix} \langle (\hat{b}^\dagger)^n \hat{b}^m \rangle_1 \\ \langle (\hat{b}^\dagger)^n \hat{b}^m \rangle_2 \end{pmatrix} = \langle \Psi | \begin{pmatrix} \langle (\hat{a}^\dagger)^n \hat{a}^m \rangle_1 \\ \langle (\hat{a}^\dagger)^n \hat{a}^m \rangle_2 \end{pmatrix} |\Psi\rangle. \tag{B8}$$

Since we are exclusively considering Gaussian states, we restrict ourselves to signal moments up to the second order [48]. They are obtained by applying the operator of Eq. (B6) to the initial signal moments with $m+n \leq 2$. With the complementary quadrature operators given by

$$\hat{q} = \frac{\hat{a} + \hat{a}^\dagger}{2}, \tag{B9}$$

$$\hat{p} = \frac{\hat{a} - \hat{a}^\dagger}{2i}, \tag{B10}$$

we define the vector $\hat{\mathbf{r}} = (\hat{q}_1, \hat{p}_1, \hat{q}_2, \hat{p}_2)$ containing the quadrature pairs of two modes, in our case. Gaussian states are fully described by the displacement vector $\hat{d}_i = \langle \hat{r}_i \rangle$ and the covariance matrix $V_{ij} = \langle \hat{r}_i \hat{r}_j + \hat{r}_j \hat{r}_i \rangle / 2 - \langle \hat{r}_i \rangle \langle \hat{r}_j \rangle$ for $i,j \in \{1,2,3,4\}$.

All quantities discussed in the main text are either evaluated directly with the signal moments, the associated first and second statistical moments, or by using the second-order correlation function [38] and interferometric power [34]. Here, we combine our model with the approach from Ref. [38] to express second-order correlation functions for arbitrary Gaussian states based on their respective covariance matrix and displacement vector. The second-order autocorrelation functions $g_1^{(2)}(0)$ and $g_2^{(2)}(0)$, as well as the second-order cross-correlation function $g_C^{(2)}(0)$ are given by

$$g_1^{(2)}(0) = 2\Bigg[2\Bigg(2(V_{11}+V_{22})^2 + 4(V_{11}+V_{22})\left(\frac{|d_1 + i\,d_2|}{\sqrt{2}}\right)^2 + \left(\left|(V_{11} - V_{22} - 2i\,V_{12}) + \left(\frac{|d_1 + i\,d_2|}{\sqrt{2}}\right)^2\right|\right)^2\Bigg) - 4\left(V_{11} + V_{22} + \left(\frac{|d_1 + i\,d_2|}{\sqrt{2}}\right)^2\right) + 1\Bigg]\Bigg[\left(2\left(V_{11} + V_{22} + \left(\frac{|d_1 + i\,d_2|}{\sqrt{2}}\right)^2\right) - 1\right)^2\Bigg]^{-1}, \tag{B11}$$

$$g_2^{(2)}(0) = 2\Bigg[2\Bigg(2(V_{33}+V_{44})^2 + 4(V_{33}+V_{44})\left(\frac{|d_3 + i\,d_4|}{\sqrt{2}}\right)^2 + \left(\left|(V_{33} - V_{44} - 2i\,V_{34}) + \left(\frac{|d_3 + i\,d_4|}{\sqrt{2}}\right)^2\right|\right)^2\Bigg) - 4\left(V_{33} + V_{44} + \left(\frac{|d_3 + i\,d_4|}{\sqrt{2}}\right)^2\right) + 1\Bigg]\Bigg[\left(2\left(V_{33} + V_{44} + \left(\frac{|d_3 + i\,d_4|}{\sqrt{2}}\right)^2\right) - 1\right)^2\Bigg]^{-1}, \tag{B12}$$

$$
\begin{aligned}
g_C^{(2)}(0) = \Bigg[& 2(A+B)^2 - 3B - 3a - 3b + \left| A - B - 2iC + \frac{(x_2+iy_2)^2}{2} \right|^2 + \frac{|x_1+iy_1|^2\,|x_2+iy_2|^2}{2} \\
& - 3A + 2\,(a+b)\,(A+B) - \frac{3\,|x_1+iy_1|^2}{2} - \frac{3|x_2+iy_2|^2}{2} + \frac{|x_2+iy_2|^2\,(4A+4B)}{2} \\
& + \left| a - b - 2ic + \frac{(x_1+iy_1)^2}{2} \right|^2 + 2|e+h+if\ -ig|^2 + 2\,(a+b)^2 \\
& + \frac{|x_1+iy_1|^2\,(4a+4b)}{2} + |x_1+iy_1|^2\,(A+B) + 2\,|h-e+if\ +ig|^2 + |x_2+iy_2|^2\,(a+b) \\
& + (x_1-iy_1)(x_2+iy_2)\,(e+h-if\ +ig) + (x_1+iy_1)\,(x_2-iy_2)\,(e+h+if\ -ig) \\
& - (x_1-iy_1)(x_2-iy_2)(h-e+if\ +ig) + (x_1+iy_1)\,(x_2+iy_2)\,(e-h+if\ +ig) + \frac{3}{2} \Bigg] \\
& \times \left[\frac{|x_1+iy_1|^2}{2} + \frac{|x_2+iy_2|^2}{2} + A + B + a + b - 1 \right]^{-2},
\end{aligned}
\tag{B13}
$$

where

$$
\begin{aligned}
&a = V_{11}, \quad b = V_{22}, \quad c = V_{12}, \quad e = V_{13}, \quad f = V_{14}, \\
&g = V_{23}, \quad h = V_{24}, \quad A = V_{33}, \quad B = V_{44}, \quad C = V_{34},
\end{aligned}
\tag{B14}
$$

and

$$
x_1 = d_1, \quad y_1 = d_2, \quad x_2 = d_3, \quad y_2 = d_4. \tag{B15}
$$

The interferometric power can be expressed as [34]

$$
\mathcal{P} = \frac{(X + \sqrt{X^2 + YZ})}{2Y}, \tag{B16}
$$

where

$$
X = (D+F)(1+E+F-G) - G^2, \tag{B17}
$$

$$
Y = (G-1)(1+D+E+2F+G), \tag{B18}
$$

$$
Z = (D+G)(DE-G) + F(2D+F)(1+E), \tag{B19}
$$

and

$$
D = 4(V_{11}V_{22} - V_{12}V_{21}), \tag{B20}
$$

$$
E = 4(V_{33}V_{44} - V_{34}V_{43}), \tag{B21}
$$

$$
F = 4(V_{13}V_{24} - V_{14}V_{23}), \tag{B22}
$$

$$
G = \det(4\mathbf{V}). \tag{B23}
$$

In the main text, we used the theoretical (reconstructed) photon number of the local mode at Out1 of our circuit to compute $\mathcal{P}_{\mathrm{SQL}} = N = (2(\sigma_q^2 + \sigma_p^2) - 1)/2$ and $\mathcal{P}_{\mathrm{HL}}$. The parameters used in the theoretical model are summarized in Tables I and II. The parameters $\varepsilon_1, \varepsilon_2$, and ε_3 are estimated from the data sheets of the respective passive microwave components. The displacement amplitudes $|\alpha_1|$ and $|\alpha_2|$ are adjusted via the photon-number calibration factor in combination with an individual two-pulsed power

TABLE I. Model parameters used for the simulated results of Figs. 3 and 4 in the main text. Each point in Figs. 3 and 4 in the main text is obtained using 1.4×10^9 raw data points. The loss values ε_j are estimated based on the respective data sheet values. The complex displacement amplitudes $\alpha_i = |\alpha_i|\exp[i(\pi/2 - \theta_i)]$ and the respective JPA parameters (r_i, n_i, γ_i) are reconstructed.

$\lvert\alpha_1\rvert^2$	θ_1	$\lvert\alpha_2\rvert^2$	θ_2	ε_1 (dB)	ϕ_1
0.723	0.639π	0.670	0 to 2π	0.63	1.31π
ϕ_2	r_1	γ_1	n_1	r_2	γ_2
1.36π	1.01(4)	0 to 2π	0.034(5)	0.723(2)	0
n_2	ε_2 (dB)	ε_3 (dB)			
0.441(9)	0.31	0.3			

TABLE II. Model parameters used for the simulated results of Fig. 5 in the main text. Each point in Fig. 5 in the main text is obtained using 2.1×10^9 raw data points per independent measurement. The listed values are derived in the same way as in Table I and averaged for 16 independent measurements.

$\lvert\alpha_1\rvert^2$	θ_1	$\lvert\alpha_2\rvert^2$	θ_2	ε_1 (dB)
0.177 to 10.76	0.806π	0.177 to 10.76	0.806π	0.63
ϕ_1	ϕ_2	r_1	γ_1	n_1
1.03π	1.36π	0.508(5)	$\pi/2$	0.0004(6)
r_2	γ_2	n_2	ε_2 (dB)	ε_3 (dB)
0.422(5)	π	0.124(4)	0.31	0.3

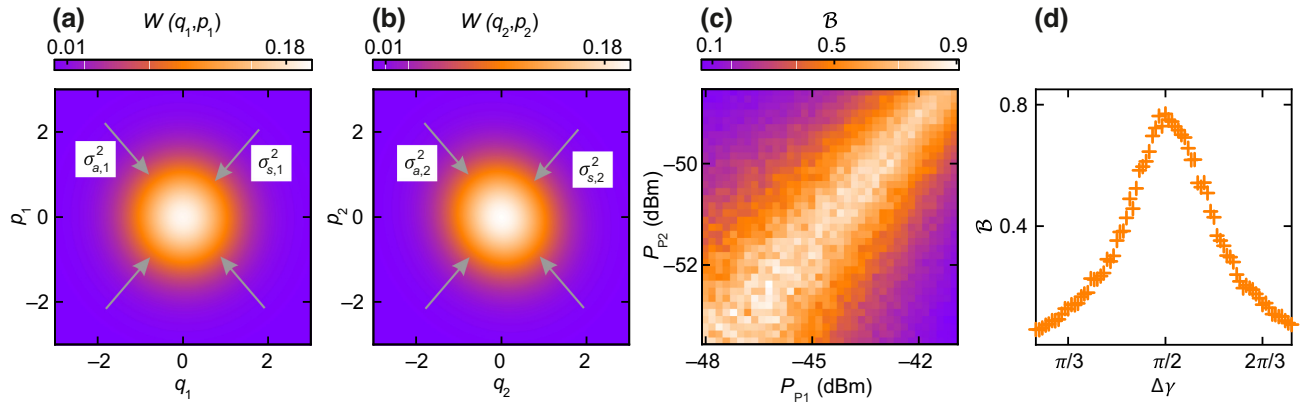

FIG. 8. Interferometer calibration. The squashed variances $\sigma^2_{s,i}$ and amplified variances $\sigma^2_{a,i}$ $(i = 1, 2)$ of the reconstructed Wigner functions $W(q_i, p_i)$ of the output fields in (a) Out1 and (b) Out2 are used to define a balancing parameter $\mathcal{B}$, which enables optimization of (c) JPA pump powers P_{P1} and P_{P2} (at the JPA ports) and (d) a relative JPA amplification orientation $\Delta\gamma = |\gamma_1 - \gamma_2|$.

sweep of the two rf sources connected to In1 and In2. The displacement angles θ_1 and θ_2 in Table I (Table II) are reconstructed and adjusted in real time using 6.248×10^8 (9.372×10^8) raw data points. The squeezing angles γ_1 and γ_2 in Table I (Table II) are processed similarly using 1.2496×10^9 (1.8744×10^9) raw data points. The reconstructed JPA squeezing factors, r_1 and r_2, are obtained in postprocessing, where the averaged demodulated data are taken into account for 46 independent measurements of 1.2496×10^9 (1.8744×10^9) raw data points, respectively. The theory model relies on ϕ_i as the free parameter, representing the phase acquired by signals in paths 1 and 2 of the interferometer, respectively.

APPENDIX C: CIRCUIT CALIBRATION

Figure 8 illustrates the concept behind the balancing parameter $\mathcal{B} = (\sigma^2_{s,1}/\sigma^2_{a,1})(\sigma^2_{s,2}/\sigma^2_{a,2})$. Figure 8(a) shows the reconstructed Wigner function of the local output Out1 of the interferometer during calibration. We analyze remaining variance asymmetries between two orthogonal quadratures $\sigma^2_{a,1}$ and $\sigma^2_{s,1}$ and try to minimize them. Similarly, as shown in Fig. 8(b), we optimize $\sigma^2_{a,2}$ versus $\sigma^2_{s,2}$. For a fixed $\Delta\gamma_{\mathrm{JPA}} = \pi/2$, we investigate $\mathcal{B}$ as a function of the level of the pump tones, P_{P1} and P_{P2}, entering the respective JPA pump port [Fig. 8(c)]. Note that $\mathcal{B}$ is unity for an ideal balanced state and decreases with increasing imbalance between the local variances. As can be seen in Fig. 8(d), the balancing is best for amplification along orthogonal orientations in phase space, i.e., $\Delta\gamma_{\mathrm{JPA}} = |\gamma_2 - \gamma_1| = \pi/2$, as expected from theory [48].

[1] P. Sibson, C. Erven, M. Godfrey, S. Miki, T. Yamashita, M. Fujiwara, M. Sasaki, H. Terai, M. G. Tanner, C. M. Natarajan, R. H. Hadfield, J. L. O'Brien, and M. G. Thompson, Chip-based quantum key distribution, Nat. Commun. **8**, 13984 (2017).

[2] C. L. Degen, F. Reinhard, and P. Cappellaro, Quantum sensing, Rev. Mod. Phys. **89**, 035002 (2017).

[3] Vittorio Giovannetti, Seth Lloyd, and Lorenzo Maccone, Quantum Metrology, Phys. Rev. Lett. **96**, 010401 (2006).

[4] Won-Young Hwang, Quantum Key Distribution with High Loss: Toward Global Secure Communication, Phys. Rev. Lett. **91**, 057901 (2003).

[5] S. Pogorzalek, K. G. Fedorov, M. Xu, A. Parra-Rodriguez, M. Sanz, M. Fischer, E. Xie, K. Inomata, Y. Nakamura, E. Solano, A. Marx, F. Deppe, and R. Gross, Secure quantum remote state preparation of squeezed microwave states, Nat. Commun. **10**, 2604 (2019).

[6] Min Xiao, Ling-An Wu, and H. J. Kimble, Precision Measurement Beyond the Shot-Noise Limit, Phys. Rev. Lett. **59**, 278 (1987).

[7] Roman Schnabel, Squeezed states of light and their applications in laser interferometers, Phys. Rep. **684**, 1 (2017).

[8] J. Abadie, B. P. Abbott, R. Abbott, T. D. Abbott, M. Abernathy, C. Adams, R. Adhikari, C. Affeldt, P. Ajith, and B. Allen, *et al.*, A gravitational wave observatory operating beyond the quantum shot-noise limit, Nat. Phys. **7**, 962 (2011).

[9] Max Born, Emil Wolf, A. B. Bhatia, P. C. Clemmow, D. Gabor, A. R. Stokes, A. M. Taylor, P. A. Wayman, and W. L. Wilcock, *Principles of Optics* (Cambridge University Press, Cambridge, 2013).

[10] Z. Y. Ou and Xiaoying Li, Quantum SU(1,1) interferometers: Basic principles and applications, APL Photonics **5**, 080902 (2020).

[11] Carlton M. Caves, Quantum-mechanical noise in an interferometer, Phys. Rev. D **23**, 1693 (1981).

[12] P. Grangier, R. E. Slusher, B. Yurke, and A. LaPorta, Squeezed-Light-Enhanced Polarization Interferometer, Phys. Rev. Lett. **59**, 2153 (1987).

[13] Vittorio Giovannetti, Seth Lloyd, and Lorenzo Maccone, Advances in quantum metrology, Nat. Photonics **5**, 222 (2011).

[14] M. Napolitano, M. Koschorreck, B. Dubost, N. Behbood, R. J. Sewell, and M. W. Mitchell, Interaction-based

quantum metrology showing scaling beyond the Heisenberg limit, Nature **471**, 486 (2011).
[15] Bernard Yurke, Samuel L. McCall, and John R. Klauder, SU(2) and SU(1,1) interferometers, Phys. Rev. A **33**, 4033 (1986).
[16] Z. Y. Ou, Fundamental quantum limit in precision phase measurement, Phys. Rev. A **55**, 2598 (1997).
[17] Z. Y. Ou, Enhancement of the phase-measurement sensitivity beyond the standard quantum limit by a nonlinear interferometer, Phys. Rev. A **85**, 023815 (2012).
[18] F. Hudelist, Jia Kong, Cunjin Liu, Jietai Jing, Z. Y. Ou, and Weiping Zhang, Quantum metrology with parametric amplifier-based photon correlation interferometers, Nat. Commun. **5**, 3049 (2014).
[19] Kirill G. Fedorov, Michael Renger, Stefan Pogorzalek, Roberto Di Candia, Qiming Chen, Yuki Nojiri, Kunihiro Inomata, Yasunobu Nakamura, Matti Partanen, Achim Marx, Rudolf Gross, and Frank Deppe, Experimental quantum teleportation of propagating microwaves, Sci. Adv. **7**, eabk0891 (2021).
[20] Shabir Barzanjeh, Saikat Guha, Christian Weedbrook, David Vitali, Jeffrey H. Shapiro, and Stefano Pirandola, Microwave Quantum Illumination, Phys. Rev. Lett. **114**, 080503 (2015).
[21] E. Flurin, N. Roch, F. Mallet, M. H. Devoret, and B. Huard, Generating Entangled Microwave Radiation Over Two Transmission Lines, Phys. Rev. Lett. **109**, 183901 (2012).
[22] R. Assouly, R. Dassonneville, T. Peronnin, A. Bienfait, and B. Huard, Quantum advantage in microwave quantum radar, Nat. Phys. (2023).
[23] U. Las Heras, R. Di Candia, K. G. Fedorov, F. Deppe, M. Sanz, and E. Solano, Quantum illumination reveals phase-shift inducing cloaking, Sci. Rep. **7**, 9333 (2017).
[24] Saikat Guha and Baris I. Erkmen, Gaussian-state quantum-illumination receivers for target detection, Phys. Rev. A **80**, 052310 (2009).
[25] Seth Lloyd, Enhanced sensitivity of photodetection via quantum illumination, Science **321**, 1463 (2008).
[26] Giacomo Sorelli, Nicolas Treps, Frederic Grosshans, and Fabrice Boust, Detecting a target with quantum entanglement, IEEE Aerosp. Electron. Syst. Mag. **37**, 68 (2022).
[27] B. Yurke, L. R. Corruccini, P. G. Kaminsky, L. W. Rupp, A. D. Smith, A. H. Silver, R. W. Simon, and E. A. Whittaker, Observation of parametric amplification and deamplification in a Josephson parametric amplifier, Phys. Rev. A **39**, 2519 (1989).
[28] T. Yamamoto, K. Inomata, M. Watanabe, K. Matsuba, T. Miyazaki, W. D. Oliver, Y. Nakamura, and J. S. Tsai, Flux-driven Josephson parametric amplifier, Appl. Phys. Lett. **93**, 042510 (2008).
[29] E. P. Menzel, R. Di Candia, F. Deppe, P. Eder, L. Zhong, M. Ihmig, M. Haeberlein, A. Baust, E. Hoffmann, D. Ballester, K. Inomata, T. Yamamoto, Y. Nakamura, E. Solano, A. Marx, and R. Gross, Path Entanglement of Continuous-Variable Quantum Microwaves, Phys. Rev. Lett. **109**, 250502 (2012).
[30] C. Eichler, D. Bozyigit, C. Lang, M. Baur, L. Steffen, J. M. Fink, S. Filipp, and A. Wallraff, Observation of Two-Mode Squeezing in the Microwave Frequency Domain, Phys. Rev. Lett. **107**, 113601 (2011).
[31] M. Renger, S. Pogorzalek, F. Fesquet, K. Honasoge, F. Kronowetter, Q. Chen, Y. Nojiri, K. Inomata, Y. Nakamura, A. Marx, F. Deppe, R. Gross, and K. G. Fedorov, Flow of quantum correlations in noisy two-mode squeezed microwave states, Phys. Rev. A **106**, 052415 (2022).
[32] M. Mariantoni, E. P. Menzel, F. Deppe, M. A. Araque Caballero, A. Baust, T. Niemczyk, E. Hoffmann, E. Solano, A. Marx, and R. Gross, Planck Spectroscopy and Quantum Noise of Microwave Beam Splitters, Phys. Rev. Lett. **105**, 133601 (2010).
[33] Kirill G. Fedorov, L. Zhong, S. Pogorzalek, P. Eder, M. Fischer, J. Goetz, E. Xie, F. Wulschner, K. Inomata, T. Yamamoto, Y. Nakamura, R. Di Candia, U. Las Heras, M. Sanz, E. Solano, E. P. Menzel, F. Deppe, A. Marx, and R. Gross, Displacement of Propagating Squeezed Microwave States, Phys. Rev. Lett. **117**, 020502 (2016).
[34] Gerardo Adesso, Gaussian interferometric power, Phys. Rev. A **90**, 022321 (2014).
[35] Davide Girolami, Alexandre M. Souza, Vittorio Giovannetti, Tommaso Tufarelli, Jefferson G. Filgueiras, Roberto S. Sarthour, Diogo O. Soares-Pinto, Ivan S. Oliveira, and Gerardo Adesso, Quantum Discord Determines the Interferometric Power of Quantum States, Phys. Rev. Lett. **112**, 210401 (2014).
[36] Kavan Modi, Aharon Brodutch, Hugo Cable, Tomasz Paterek, and Vlatko Vedral, The classical-quantum boundary for correlations: Discord and related measures, Rev. Mod. Phys. **84**, 1655 (2012).
[37] K. G. Fedorov, S. Pogorzalek, U. Las Heras, M. Sanz, P. Yard, P. Eder, M. Fischer, J. Goetz, E. Xie, K. Inomata, Y. Nakamura, R. Di Candia, E. Solano, A. Marx, F. Deppe, and R. Gross, Finite-time quantum entanglement in propagating squeezed microwaves, Sci. Rep. **8**, 6416 (2018).
[38] Stefano Olivares, Simone Cialdi, and Matteo G. A. Paris, Homodyning the g(2)(0) of Gaussian states, Opt. Commun. **426**, 547 (2018).
[39] E. D. Lopaeva, I. Ruo Berchera, I. P. Degiovanni, S. Olivares, G. Brida, and M. Genovese, Experimental Realization of Quantum Illumination, Phys. Rev. Lett. **110**, 153603 (2013).
[40] Zheshen Zhang, Maria Tengner, Tian Zhong, Franco N. C. Wong, and Jeffrey H. Shapiro, Entanglement's Benefit Survives an Entanglement-Breaking Channel, Phys. Rev. Lett. **111**, 010501 (2013).
[41] Zheshen Zhang, Sara Mouradian, Franco N. C. Wong, and Jeffrey H. Shapiro, Entanglement-Enhanced Sensing in a Lossy and Noisy Environment, Phys. Rev. Lett. **114**, 110506 (2015).
[42] Zihao Gong, Nathaniel Rodriguez, Christos N. Gagatsos, Saikat Guha, and Boulat A. Bash, Quantum-enhanced transmittance sensing, IEEE J. Sel. Top. Signal Process. **17**, 473 (2022).
[43] Yannis K. Semertzidis, SungWoo Youn, and 'Axion dark matter, How to see it?', Sci. Adv. **8**, eabm9928 (2022).
[44] C. M. Adair, K. Altenmüller, V. Anastassopoulos, S. Arguedas Cuendis, J. Baier, K. Barth, A. Belov,

D. Bozicevic, and H. Bräuninger, *et al.*, Search for dark matter axions with CAST-CAPP, Nat. Commun. **13**, 6180 (2022).

[45] Shao-Hua Xiang, Wei Wen, Yu-Jing Zhao, and Ke-Hui Song, Evaluation of the non-Gaussianity of two-mode entangled states over a bosonic memory channel via cumulant theory and quadrature detection, Phys. Rev. A **97**, 042303 (2018).

[46] M. Renger, S. Pogorzalek, Q. Chen, Y. Nojiri, K. Inomata, Y. Nakamura, M. Partanen, A. Marx, R. Gross, F. Deppe, and K. G. Fedorov, Beyond the standard quantum limit for parametric amplification of broadband signals, npj Quantum Inf. **7**, 160 (2021).

[47] Note that this is only a symbolic notation for better clarity. For a full description, the environment enters via two additional modes. Since we do not care further about the environment, we drop these modes.

[48] Samuel L. Braunstein and Peter van Loock, Quantum information with continuous variables, Rev. Mod. Phys. **77**, 513 (2005).